Acta Cryst B
STRUCTURAL SCIENCE
CRYSTAL ENGINEERING
MATERIALS
ISSN 2052-5206

Experimental and theoretical charge-density analysis of hippuric acid: insight into its binding with human serum albumin

Asma Hasil,[a] Arshad Mehmood[b] and Maqsood Ahmed[a]*

[a]Materials Chemistry Laboratory, Department of Chemistry, The Islamia University of Bahawalpur, Baghdad-ul-Jadeed Campus 63100, Pakistan, and [b]Department of Chemistry and Biochemistry, Texas Christian University, Fort Worth, Texas 76129, USA. *Correspondence e-mail: maqsood.ahmed@iub.edu.pk

Received 13 March 2019
Accepted 2 June 2019

Edited by P. Macchi, University of Bern, Switzerland

Keywords: hippuric acid (HA); human serum albumin (HSA); kidney failure; uremic toxins; metabolites; charge-density analysis; dipole-moment calculations; electrostatic potential; *MoPro*.

Supporting information: this article has supporting information at journals.iucr.org/b

In order to comprehend the binding of an important metabolite, hippuric acid, with human serum albumin and to understand its chemical and electronic nature, an experimental charge-density analysis has been carried out using high-resolution diffraction data collected under cryogenic conditions, and all the results have been compared with theoretical findings using the B3LYP/6-311++g(2d,2p) level of theory. The structure displays very strong classical hydrogen bonds as well as other noncovalent interactions, which have been fully characterized using Hirshfeld surface analysis and Bader's quantum theory of atoms in molecules. Contact analysis on the Hirshfeld surfaces shows that the O···H, C···H and C···N intermolecular interactions are enriched and gives their relative strengths. Topological analysis of the electron density shows the charge concentration/depletion of hippuric acid bonds in the crystal structure. Electrostatic parameters such as atomic charges and dipole moments were calculated. The mapping of atomic basins and the calculation of respective charges show the atomic volumes of each atom as well as their charge contributions in the hippuric acid crystal structure. The dipole-moment calculations show that the molecule is very polar in nature. Calculations of the electrostatic potential show that the chain part of the molecule has a higher concentration of negative charge than the ring, which might be instrumental in its strong binding with the polar residues of site II of human serum albumin.

1. Introduction

During kidney failure, the toxic compounds of urine that are retained in the blood are called 'uremic toxins' and they negatively affect the normal biological functioning of the body (Miyamoto *et al.*, 2010). Hippuric acid (HA) is one of these uremic toxins which causes the stimulation of ammoniagenesis after its accumulation in the blood. HA restricts the utilization of glucose by the muscles and is involved in generating muscular weakness in uraemia (Duranton *et al.*, 2012; Dzúrik *et al.*, 2001; Spustová *et al.*, 1991). It also inhibits the secretion of organic anions by the kidney (Boumendil-Podevin *et al.*, 1975) and the blood-to-brain transport barrier (Ohtsuki *et al.*, 2002). For this reason, HA is a compound of pharmacological concern. It is the biotransformed product of hepatic conjugation of glycine with benzoate, which is taken either directly from beverages and food preservatives or from aromatic phenolic acids by gastrointestinal flora (Niwa, 1996). Its concentration has been found to be less than 5 mg l^{-1} in healthy individuals and higher than 247 ± 112 mg l^{-1} in end-stage renal patients (Vanholder *et al.*, 2003).

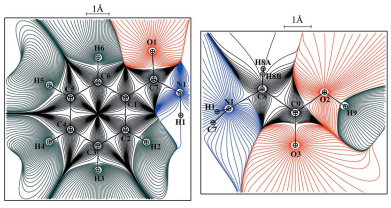

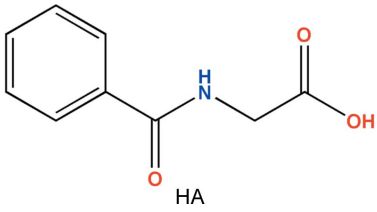

Human serum albumin (HSA) is the most abundant single-chain plasma protein, a nonglycosylated polypeptide of 66.5 kDa. The principal ligand-binding regions of HSA are located in hydrophobic cavities (Sugio *et al.*, 1999; Peters, 1995; He & Carter, 1992; Sudlow *et al.*, 1975). These binding sites of HSA underline its exceptional ability to interact with inorganic and organic molecules. The protein binds with a variety of endogenous ligands, as well as many commonly used nonsteroidal anti-inflammatory drugs (NSAIDs) and anticoagulants, such as warfarin (Petitpas *et al.*, 2001), diazepam, ibuprofen, propofol, halothane, azapropazone, phenylbutazone, indomethacin *etc.* (Bhattacharya *et al.*, 2000; Ghuman *et al.*, 2005). All of these commonly used drugs have acidic and electronegative features and bind with one of the two primary binding sites of this transport protein (Ghuman *et al.*, 2005). Therefore, HSA is an important regulator of intercellular fluxes and is also important in the regulation of the pharmacokinetic behaviour of drugs in the body (Varshney *et al.*, 2011).

Besides these features, the HSA protein also binds to the HA metabolite of uremic toxins in the body (HA also has acidic and electronegative features) (Duranton *et al.*, 2012) and thus only 64% of the latter is eliminated through haemodialysis (Vanholder *et al.*, 1992; Hung & Chang, 2001). A comprehensive study involving isothermal titration calorimetry (ITC), differential scanning calorimetry (DSC), molecular docking, circular dichroism (CD) and fluorescence spectroscopy was carried out to uncover the hampered elimination of HA during haemodialysis as a result of its binding with HSA (Zaidi *et al.*, 2013). The results of the calorimetric and docking analyses revealed that, although HA binds at two drug-binding sites, namely Sudlow's sites I and II of HSA (Sudlow *et al.*, 1975), the affinity of binding to site II was greater than that to site I. This report intends to explain this preferential binding with one of the two sites through a charge-density perspective. A detailed molecular structure analysis is needed to understand the low and high binding affinities of HA with sites I and II, respectively, of serum plasma protein via electrostatic, hydrophobic and hydrogen-bonding interactions (Zaidi *et al.*, 2013).

An analysis of topological and electrostatic properties derived from the electron-density distribution has proven to be very useful (Grabowsky *et al.*, 2008, 2007; Bouhmaida *et al.*, 2009; Yearley *et al.*, 2007) as the strength of metabolite–receptor interactions depends mainly on the electron-density distribution. Experimental electron-density studies of various drugs and biomolecules, such as estrone (Zhurova *et al.*, 2006), genistein (Yearley *et al.*, 2007), olefin, aziridine and oxirane (Grabowsky *et al.*, 2008), paracetamol (Bouhmaida *et al.*, 2009), 17α-estradiol 0.5H_2O (Zhurova *et al.*, 2009), aspirin (Arputharaj *et al.*, 2012), ethionamide (Rajalakshmi, Pavan & Kumaradhas, 2014), pyrazinamide (Rajalakshmi, Hathwar & Kumaradhas, 2014*b*), isoniazid (Rajalakshmi, Hathwar & Kumaradhas, 2014*a*), 16α,17β-estriol (Zhurova *et al.*, 2016), 2-nitroimidazole (Kalaiarasi *et al.*, 2016), andrographolide (Manjula *et al.*, 2018) and many others have been carried out and successfully established the importance of electron-density studies for understanding the chemical nature of a molecule.

The electrostatic and structural complementarity of a drug molecule with receptor-site amino acid residues is the foundation for molecular recognition. The multipole model of experimental electron density adequately explains the directional effects of these polar interactions (Muzet *et al.*, 2003). An electron-density analysis helps in determining the mode of action of a drug molecule by marking the reactive sites of the molecule (Grabowsky *et al.*, 2007, 2008). An electron-density analysis of HA will help to determine the behaviour of this metabolite molecule in the biological environment. Accurate experimental determination of the electrostatic properties of the HA molecule can reveal very valuable information about the reaction sites and binding affinities. This precise knowledge of the HA molecule could help to find a new route to designing new agents against its binding to HSA.

In the present study, the experimental electron-density distribution of HA is determined from high-resolution X-ray diffraction data at a low temperature of 100 (1) K. The electron density, the Laplacian of the electron-density distribution and the electrostatic properties, *i.e.* the atomic charges and electrostatic potentials are calculated for HA. Topological analysis of the strong and weak intermolecular interactions of the HA molecule in the crystal structure has also been carried out. The experimental results are compared with the corresponding theoretical solid-state quantum chemical calculations using density functional theory (DFT).

2. Experimental

2.1. Crystallization and data collection

The title compound (HA) was purchased from a commercial supplier and used without further purification. It was crystallized by the slow evaporation of a concentrated solution in a mixture of ethanol–methanol solvents in 1:1 stoichiometric ratio at room temperature. Colourless block-shaped crystals were obtained after a few days. A single crystal with dimensions 0.18 × 0.21 × 0.28 mm was used for the diffraction experiment. High-resolution single-crystal X-ray diffraction data were collected at 100 (1) K using Mo $K\alpha$ radiation (λ = 0.71073 Å) from a microfocus source on a Bruker D8 Venture diffractometer equipped with a PHOTON II detector. The crystal was mounted on a glass needle using vacuum grease and placed on a four-circle goniometer head under a stream of compressed nitrogen using an Oxford Cobra device to cool from room temperature to 100 K for the entire experiment. The Cobra device provided excellent temperature stability

Table 1
Experimental details.

Crystal data			
Chemical formula	$C_9H_9NO_3$		
M_r	179.17		
Crystal system, space group	Orthorhombic, $P2_12_12_1$		
Temperature (K)	100		
a, b, c (Å)	8.6793 (4), 9.0674 (4), 10.6085 (4)		
V (Å^3)	834.88 (6)		
Z	4		
Radiation type	Mo $K\alpha$		
μ (mm^{-1})	0.11		
Crystal size (mm)	0.28 × 0.21 × 0.18		
Data collection			
Diffractometer	Bruker D8 Venture with PHOTON II detector		
Absorption correction	Multi-scan (*SADABS*; Bruker, 2016)		
T_{min}, T_{max}	0.971, 0.981		
No. of measured, independent and observed reflections	118392, 13635, 11897		
R_{int}	0.058		
(sin $\theta/\lambda)_{max}$ (Å^{-1})	1.250		
Weighting scheme	$w = 1/[\delta^2{F_o}^2 + (aP)^2 + bP]$, where $P = ({F_o}^2 + 2{F_c}^2)/3$ (a = 0.0059 and b = 0.0083)		
Refinement	Multipolar	IAM_MoPro	IAM_shelx
$R[F^2 > 2\sigma(F^2)]$, $wR(F^2)$, S	0.028, 0.043, 0.97	0.040, 0.106, 1.08	0.036, 0.107, 1.11
No. of parameters	1493	118	126
H-atom treatment	H atoms treated by a mixture of independent and constrained refinement	H atoms treated by a mixture of independent and constrained refinement	H atoms treated by a mixture of independent and constrained refinement
$\Delta\rho_{max}$, $\Delta\rho_{min}$ (e Å^{-3})	0.27, −0.28	0.55, −0.38	0.51, −0.30
Absolute structure	Flack parameter x determined using 4564 quotients $[(I^+) - (I^-)]/[(I^+) + (I^-)]$ (Parsons *et al.*, 2013)	Flack parameter x determined using 4564 quotients $[(I^+) - (I^-)]/[(I^+) + (I^-)]$ (Parsons *et al.*, 2013)	Flack parameter x determined using 4564 quotients $[(I^+) - (I^-)]/[(I^+) + (I^-)]$ (Parsons *et al.*, 2013)
Absolute structure parameter	−0.05 (11)	−0.05 (11)	−0.05 (11)

better than ±1 K during the entire experiment. Bragg intensities were collected using 1.0° ω and φ scan widths. Two different exposure times of 5 and 10 s per frame were used for low and high angles, respectively, resulting in a total of 118 392 reflections up to sin θ/λ_{max} = 1.25 Å^{-1}. The *SAINT* program was used for cell refinement and reduction of data (Bruker, 2016). A multi-scan absorption correction was carried out using the *SADABS* program (Krause *et al.*, 2015).

2.2. Structure solution and refinement

Crystal data, data collection and structure refinement details are summarized in Table 1.

2.2.1. Structure solution and IAM *SHELX* refinement. The crystal structure was solved in the orthorhombic crystal system with space group $P2_12_12_1$ using the *SIR92* software (Altomare *et al.*, 1993). *SHELXL* (Sheldrick, 2015) was used initially for independent-atom-model (IAM) refinement. All the H atoms were clearly visible in the difference maps. However, a riding model (Allen & Bruno, 2010) was used for the H atoms attached to carbon, Csp^2—H = 0.95 Å and Csp^3—H = 0.99 Å, while H atoms attached to N and O atoms were refined freely. The absolute structure was determined from the Flack parameter (Flack, 1983), and the value of −0.05 (11) confirmed that the given configuration is correct. At the end of the *SHELXL* refinement the R factor was 0.036, the weighted R factor was 0.107 and the goodness of fit was 1.11. The highest difference peak and deepest hole were 0.51 and −0.30 e Å^{-3}, respectively.

2.2.2. IAM *MoPro* refinement. The refined model from the previous *SHELX* refinement was imported to the *MoPro* (*MoPro_1805_win*) software package (Jelsch *et al.*, 2005). An IAM refinement was carried out with a full-matrix least-squares refinement using intensity data up to sinθ/λ_{max} = 1.250 Å^{-1}. The same weighting scheme was used as in the previous *SHELXL* refinement: $w = 1/[\delta^2 F_o^2 + (aP)^2 + bP]$, where $P = (F_o^2 + 2F_c^2)/3$, with a = 0.0059 and b = 0.0083. Initially the scale factor was refined, followed by refinement of the positions (x, y, z) of all atoms and their displacement parameters (U_{ij}). The bond distances for C—H atoms were constrained to the standard values from neutron data (Allen & Bruno, 2010). However, the computed distances from the optimized geometry (Table S1 in the supporting information; details of the optimization procedure are given below) gave a slightly better R factor and so were used for the *MoPro* refinements. The anisotropic displacement parameters for the H atoms were constrained to calculated values from the SHADE server (Madsen, 2006). The scattering factors for C, H, N and O are taken from the Atomic Data and Nuclear Data Tables (Clementi & Roetti, 1974) and the refinement was continued to convergence. The residual electron-density maps after the IAM refinement are shown in Fig. 1. After IAM refinement with *MoPro*, the R factor was 0.0402, the weighted R factor was 0.106 and the goodness of fit was 1.08. The

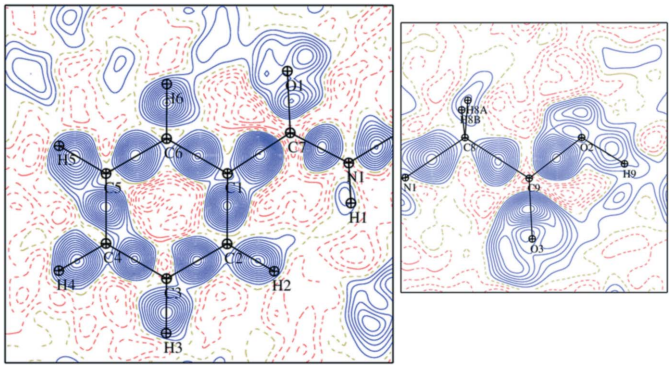

Figure 1
Residual electron-density maps for (left) the ring part of the HA molecule and (right) the chain part, after IAM refinement with *MoPro* at the 0.05 e Å^{-3} level and with sinθ/λ = 0.9 Å^{-1}.

minimum and maximum electron-density peaks and r.m.s. values were −0.38, 0.55 and 0.08 e Å^{-3}, respectively.

2.2.3. Multipolar refinement. The final model from the previous IAM refinement was used for multipolar refinement using *MoPro* on the basis of the Hansen–Coppens (Hansen & Coppens, 1978) multipolar atom model (MAM). According to this model, the electron densities of pseudo-atoms of the molecule are represented by the core electron density (ρ_{core}), the valence electron density ($\rho_{valence}$) and the aspherical part of the atomic electron density, with a spherical atom expansion and contraction coefficient κ in the valence shell. The valence electron density is given in term of spherical harmonics, and the radial expansion and contraction parameters (κ and κ') of the valence shell are given in equation (1):

$$\rho(\mathbf{r}) = \rho_{core}(r) + P_{val}\kappa^3\rho_{val}(\kappa r) + \sum_{l=0}^{l_{max}} \kappa'^3 R_{n_l}(\kappa' r) \sum_{m=0}^{l} P_{lm} y_{lm\pm}(\theta, \varphi). \quad (1)$$

The coordinates and displacement parameters of all non-H atoms were refined using all diffraction data. All the intensities up to d = 0.4 Å (sinθ/λ = 1.25 Å^{-1}) resolution were used in the refinement (no I/σ cutoff was applied). The same weighting scheme was used as described in previous sections. The resolution dependence of the data and model quality was monitored by *DRK* plots (Zhurov *et al.*, 2008) (Fig. S1 in the supporting information).

The following strategy was used in the multipolar refinement:

(i) H atoms were treated as in the previous section.

(ii) The κ parameters for H atoms were restrained to 1.16 (2).

(iii) Subsequently, the valence population P_{val} parameter and multipole population parameter $P_{lm\pm}$ were refined successively. The H atoms were refined to dipolar level whereas all the other atoms were refined to octapolar level. In the last cycles of the refinement, all parameters were simultaneously refined together to convergence.

As a result of the MAM refinement, the R factor was 0.0281, the weighted R factor was 0.0425 and the goodness of fit was 0.965. The minimum and maximum electron-density peaks and r.m.s. values were −0.28, 0.27 and 0.06 e Å^{-3}, respectively.

2.3. Theoretical calculations

Two types of theoretical calculation were carried out:

(i) Atomic coordinates obtained after multipolar refinement using the neutron diffraction bond lengths of H atoms were taken as the starting geometry to optimize the positions of the H atoms in the crystal structure. Periodic electronic structure calculations were carried out at the general gradient approximation (GGA) level using the Perdew–Burke–Ernzerhof (PBE) functional (Perdew *et al.*, 1996) in combination with Grimme's D3 correction for dispersion interactions (Grimme *et al.*, 2010) employing the Gaussian plane wave (GPW) formalism implemented in the *QUICKSTEP* module of the *CP2K* program suite (Version 5.1; Hutter *et al.*, 2014). The molecular orbitals of all atomic species were expanded in the 6-311G** basis set and the core–valence-shell electron interactions were described by Goedecker–Teter–Hutter (GTH) pseudo-potentials (Hartwigsen *et al.*, 1998). The periodic boundary conditions (PBC) were applied in three dimensions using the fixed unit-cell parameters obtained from the experimental crystal structures and only H atoms were allowed to relax during the optimization process. The plane-wave basis set was truncated at a cut off of 450 Ry and the reference grid was cut off at 75 Ry at the default multi-grid level of 4. The maximum force and self-consistent field (SCF) convergence criterion were set to 10^{-4} Hartree Bohr^{-1} and 10^{-8} E_h, respectively. The obtained optimized hydrogen-bond lengths were used in the *MoPro* refinement of experimental models.

(ii) The final coordinates obtained after the multipolar refinement were used as the input geometry for single-point energy calculations using the *GAUSSIAN09* suite of programs (Frisch *et al.*, 2009) at the B3LYP/6-311++g(2d,2p) level. The obtained molecular wavefunction was used to calculate the deformation density, integrated theoretical population and atomic volumes using the *Multiwfn* program (Version 3.6; Lu & Chen, 2012). To avoid the orientation dependence problem in pro-molecular density, the calculated electron density of each atom was artificially sphericalized, *e.g.* by replacing the s^2p^2 ground-state configuration of carbon with sp^3 and by setting the occupation number of the 2p orbitals of oxygen to 4/3. The calculations of bond-critical points (BCPs) and theoretical topological properties at the BCPs, atomic basins and gradient paths were performed with the *AIM-UC* program (Vega & Almeida, 2014).

3. Results and discussion

3.1. Molecular structure

The crystal structure of HA was previously reported by Ringertz (1971) at room temperature. In the present study, we have redetermined the crystal structure of HA at low temperature (100 K) to perform the charge-density analysis. The current study reports a bond precision to 10^{-4} Å, versus

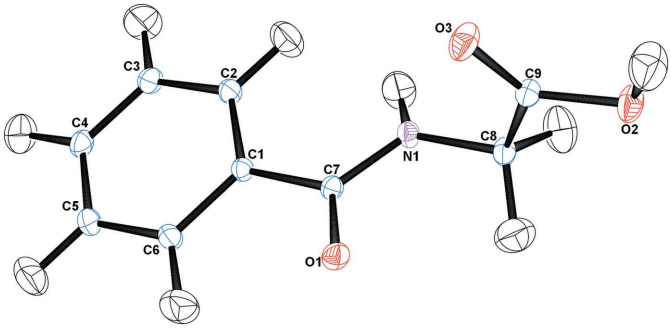

Figure 2
A displacement ellipsoid plot of the HA molecule drawn at the 50% probability level, showing the atom-numbering scheme for non-H atoms (*ORTEPIII*; Johnson & Burnett, 1996; Farrugia, 1997).

10^{-3} Å in the previous study. Fig. 2 shows a displacement ellipsoid plot of the molecule with the atom-numbering scheme. The geometric parameters of both the IAM and the multipolar model of the molecule are given in the supporting information.

The unit-cell packing along the *b* and *c* axes is shown in Figs. 3(*a*) and 3(*b*). The molecules are stacked above each other along the *b* axis, while along the *c* axis the molecules are packed in a net-like zigzag arrangement. The dihedral angle between the plane of the aromatic benzene ring and that of atoms O1, C7 and N1 is 11.25 (3)°, indicating that these are not coplanar. Similarly, the –COOH functional group is oriented almost perpendicular to the plane of the aromatic ring, with the dihedral angle between their respective planes being 84.53°.

The crystal structure of HA is stabilized by strong and weak intermolecular interactions. All the heteroatoms are involved in the formation of classical hydrogen bonds except O3, which forms four C—H···O hydrogen-bond interactions. Each HA molecule forms four moderately strong hydrogen-bond interactions (O—H···O and N—H···O) with its neighbouring symmetry-related molecules. Carbonyl O1 forms two classical bifurcated hydrogen-bond interactions by accepting atoms H2 and H9 from atoms N1 and O2 of neighbouring molecules.

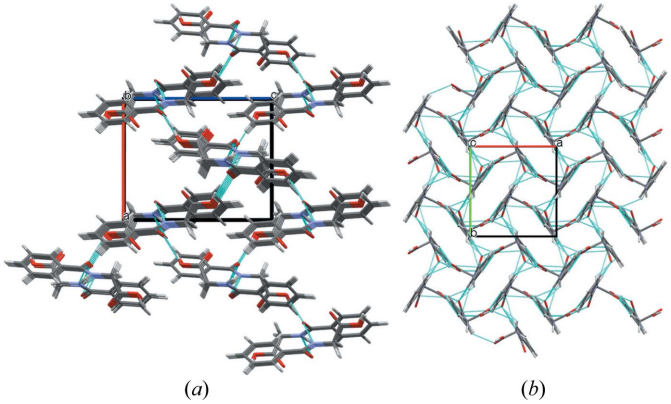

Figure 3
A view of the molecular packing along (*a*) the *b* axis and (*b*) the *c* axis. The turquoise lines show the strong hydrogen bonds.

Table 2
Hydrogen-bond geometry (Å, °) for the multipolar model.

D—H···*A*	*D*—H	H···*A*	*D*···*A*	*D*—H···*A*
C8—H8*B*···O3^{i}	1.10	2.54	3.5953 (3)	161
C4—H4···O2^{ii}	1.09	2.57	3.1810 (3)	114
N1—H1···C2	1.02	2.55	2.9197 (3)	101
O2—H9···O1^{iii}	1.00	1.67	2.6544 (3)	165
C2—H2···O1^{iv}	1.09	2.38	3.4411 (3)	166
C8—H8*A*···C6^{iv}	1.10	2.74	3.4842 (4)	125
N1—H1···O1^{iv}	1.02	1.99	2.9561 (3)	156

Symmetry codes: (i) $x-\frac{1}{2}, -y+\frac{3}{2}, -z+2$; (ii) $x, y, z-1$; (iii) $x+\frac{1}{2}, -y+\frac{3}{2}, -z+2$; (iv) $-x+1, y-\frac{1}{2}, -z+\frac{3}{2}$.

Table 2 lists all the intermolecular strong and weak hydrogen-bonding parameters of the HA molecule from the multipolar model with the respective symmetry codes.

3.2. Hirshfeld surface and fingerprint analysis

To understand the intermolecular interactions it is necessary to have knowledge of the interacting surface of a drug/metabolite with its biological environment. The Hirshfeld surface allows us to quantify the various intermolecular interactions contributing to the packing of a whole molecule in a crystal structure (Spackman & Jayatilaka, 2009; McKinnon *et al.*, 2007). The Hirshfeld surface of the HA molecule was mapped with $d_{\rm norm}$ (Fig. 4) using *Crystal Explorer* (Turner *et al.*, 2017) in which white shading shows contacts which are close to the van der Waals radii, blue indicates longer contacts and red represents the stronger interactions present in the crystal structure of HA. In the surface map the dark-red region in the vicinity of O2 and O1 shows the presence of strong O2—H9···O1^{iv}, C4—H4···O2^{iii}, C4—H4···O3^{i} and C8—H8B···O3^{ii} intermolecular interactions in the crystal structure, as well as weak C5—H5···O3^{i} and C8—H8A···C6^{v} intermolecular interactions (symmetry codes are same as in Table 2). These colour indications are very useful to identify and establish the relative strength of possible intermolecular interactions between the HA molecule and its biological environment, as well as to determine the molecular environment of the crystal space.

Fingerprint plots analyse the intermolecular interactions and molecular packing in a crystal structure on the basis of the Hirshfeld surface (McKinnon *et al.*, 2004; Spackman &

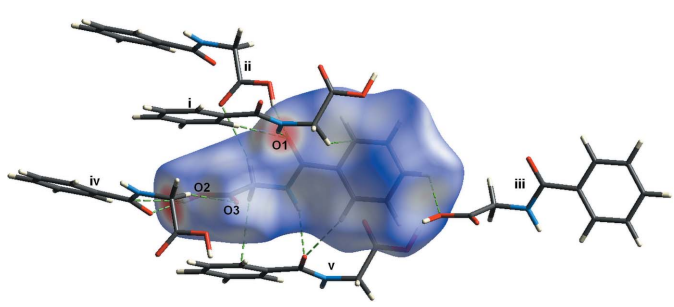

Figure 4
A diagram of the Hirshfeld surface of the parent HA molecule, showing the interacting molecules. Symmetry codes are given in Table 2.

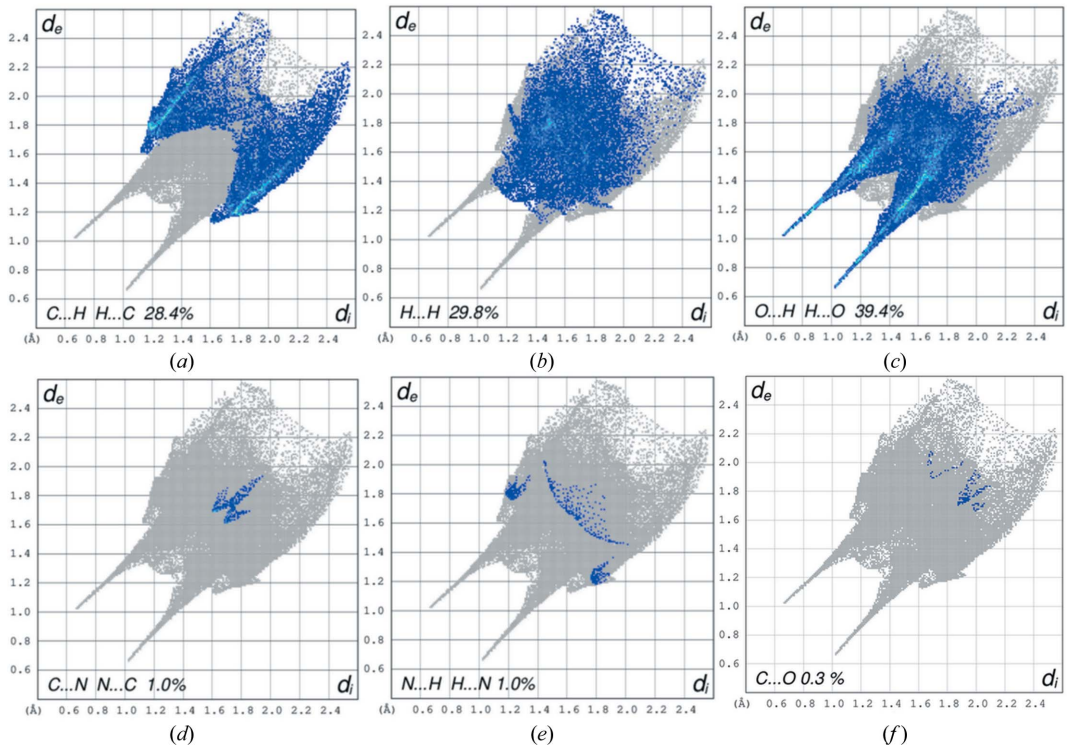

Figure 5
Fingerprint plots showing the percentages of interactions present in the HA molecule.

Jayatilaka, 2009; Turner *et al.*, 2017). Fingerprint plots of the HA molecule were mapped with d_{norm} using *Crystal Explorer* and are shown in Fig. 5, where sharp spikes show the presence of O···H contacts contributing 39.4% of the total interactions and broader areas represent the presence of H···H contacts with a respective contribution of 29.8%. The appearance of wing-shaped fingerprint plots in Fig. 5 shows the presence of C···H contacts which make a considerable contribution of 28.4% to the interactions. Furthermore, among the lesser to weak interactions C···N, N···H, C···O and C···C, the C···N and N···H ones contribute only 1%. This C···N contact is one of the most important for the crystal packing of HA, although it contributes only 0.9% of the total interactions, while the C···O and C···C contacts make a negligible/weak contribution of 0.02%. The enrichment ratio factor (EF) was calculated using the technique provided by Jelsch *et al.* (2014) and shows that the C···N, O···H and C···H interactions are the favoured ones in the crystal packing of HA as their corresponding EF values are 3.322, 1.546 and 1.469, respectively. Overall, the O···H, H···H and C···H contributions make a significantly greater contribution than C···N, N···H, C···O and C···C to the total percentile of the Hirshfeld surface. The Hirshfeld surface map enables us to understand the intermolecular interactions and the strength of the above-mentioned strong and weak interactions contributing to the surface of the HA molecule.

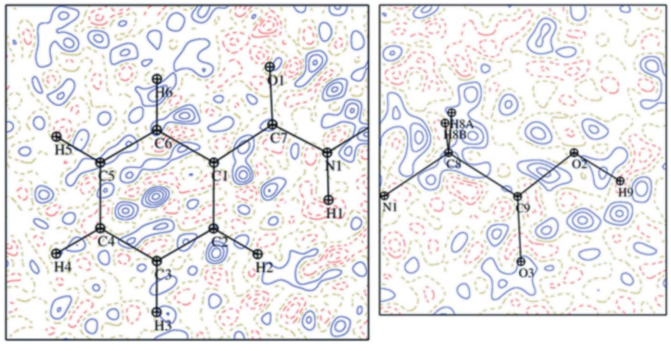

Figure 6
Residual electron-density maps for (left) the ring part of the HA molecule and (right) the chain part, after multipolar refinement. Contour level 0.05 e Å^{-3}, sinθ/λ = 1 Å^{-1}.

3.3. Topological analysis of electron density

The residual density map and the rigid-bond test (Hirshfeld, 1976) were used to determine the quality of the refined model. These residual density maps (Fig. 6) represent very good agreement between the observed and calculated electron densities.

The static deformation density maps (Fig. 7) represent the charge accumulation, the positions of the lone pairs of the N and O atoms and the shape of the bonding regions in the HA molecule. A BCP search was carried out in the molecule and revealed the presence of (3,−1) BCPs, confirming the presence of covalent interactions in the bonds of the HA molecule. It is important to note that we get fine details about the strength of the intermolecular interactions by studying the topological properties rather than relying merely on the geometry of the molecule. Fig. S2 shows a molecular graph of

Table 3
Topological properties of (3, −1) CPs in the covalent interactions of HA: distances (Å), electron density (e Å^{-3}), Laplacian (e Å^{-5}), Hessian eigenvalues (e Å^{-5}), ε = ellipticity, G_{CP} = bond kinetic-energy density (kJ mol^{-1} Bohr^{-3}) and V_{CP} = bond potential-energy density (kJ mol^{-1} Bohr^{-3}).

The upper line in each pair gives the experimental values and the lower one the theoretical values.

No.	Bond	d_{12}	d_{1CP}	d_{2BCP}	$\rho_{BCP}(r)$	$\nabla^2\rho_{BCP}(r)$	λ_1	λ_2	λ_3	ε	G_{CP}	V_{CP}
1	C1—C2	1.403	0.730	0.673	2.118	−16.73	−16.14	−13.26	12.66	0.218	789.2	−2034
		1.403	0.702	0.701	2.067	−20.36	−16.04	−13.61	9.283	0.178	805.8	−1057
2	C2—C3	1.395	0.708	0.687	2.200	−19.64	−16.93	−13.93	11.23	0.215	807.8	−2151
		1.395	0.702	0.693	2.096	−21.12	−16.42	−13.88	9.178	0.183	831.9	−1089
3	C3—C4	1.397	0.689	0.708	2.141	−19.55	−16.55	−13.70	10.70	0.208	757.8	−2048
		1.397	0.698	0.699	2.093	−21.11	−16.39	−13.95	9.232	0.175	828.6	−1082
4	C4—C5	1.396	0.668	0.728	2.185	−20.03	−17.00	−13.99	10.96	0.215	787.5	−2121
		1.396	0.695	0.701	2.097	−21.22	−16.43	−14.03	9.240	0.171	831.1	−1084
5	C5—C6	1.393	0.707	0.686	2.208	−21.52	−17.38	−13.95	9.810	0.246	780.9	−2148
		1.393	0.697	0.696	2.112	−21.51	−16.56	−14.12	9.180	0.173	843.5	−1101
6	C1—C6	1.401	0.709	0.692	2.091	−17.81	−15.85	−12.92	10.96	0.227	746.1	−1977
		1.401	0.707	0.694	2.079	−20.77	−16.20	−13.86	9.288	0.169	815.4	−1065
7	C1—C7	1.492	0.719	0.773	1.862	−15.06	−14.17	−11.84	10.94	0.197	608.1	−1626
		1.492	0.731	0.761	1.782	−15.37	−13.41	−12.24	10.28	0.096	575.8	−732.9
8	C2—H2	1.088	0.717	0.371	1.851	−16.80	−17.26	−16.64	17.10	0.037	568.0	−1593
		1.086	0.686	0.400	1.929	−25.42	−18.88	−18.62	12.08	0.013	800.5	−908.5
9	C3—H3	1.089	0.748	0.341	1.838	−19.33	−18.14	−17.27	16.08	0.050	511.3	−1549
		1.089	0.694	0.396	1.924	−25.34	−19.00	−18.71	12.37	0.016	790.4	−890.5
10	C4—H4	1.086	0.737	0.349	1.879	−19.45	−18.07	−17.95	16.57	0.007	542.1	−1614
		1.089	0.694	0.395	1.926	−25.41	−19.02	−18.79	12.41	0.013	791.2	−890.1
11	C5—H5	1.087	0.731	0.357	1.838	−18.08	−18.11	−16.73	16.76	0.082	534.2	−1561
		1.086	0.691	0.394	1.944	−25.89	−29.30	−19.03	12.43	0.014	806.0	−906.8
12	C6—H6	1.088	0.726	0.363	1.822	−17.23	−17.02	−16.05	15.83	0.060	537.4	−1544
		1.088	0.703	0.385	1.952	−26.14	−16.69	−16.49	13.05	0.011	803.6	−895.3
13	C7═O1	1.254	0.437	0.816	2.768	−30.51	−24.71	−23.81	18.01	0.038	1153	−3136
		1.254	0.443	0.810	2.635	−21.18	−23.83	−21.62	24.57	0.102	1760	−2943
14	C7—N1	1.336	0.502	0.834	2.396	−29.05	−20.00	−16.38	7.330	0.221	814.5	−2420
		1.336	0.507	0.829	2.299	−27.27	−19.74	−17.05	9.526	0.158	1303	−1863
15	N1—H1	1.023	0.773	0.250	2.146	−28.94	−28.56	−26.99	26.61	0.058	590.9	−1970
		1.020	0.743	0.277	2.288	−39.49	−30.85	−29.30	20.66	0.053	1224	−1374
16	C8—N1	1.445	0.608	0.837	1.869	−12.15	−13.17	−12.93	13.96	0.019	666.3	−1664
		1.445	0.593	0.852	1.807	−17.36	−13.15	−12.68	8.481	0.037	767.7	−1063
17	C8—H8*A*	1.095	0.700	0.396	1.790	−16.52	−16.04	−15.31	14.83	0.047	525.5	−1501
		1.096	0.701	0.395	1.910	−24.71	−19.02	−18.34	12.65	0.037	775.4	−877.8
18	C8—H8*B*	1.098	0.732	0.366	1.781	−15.94	−16.26	−15.55	15.87	0.046	528.8	−1492
		1.099	0.714	0.385	1.907	−24.77	−19.27	−18.73	13.24	0.028	767.3	−860.1
19	C8—C9	1.517	0.692	0.826	1.752	−14.11	−13.12	−10.84	9.850	0.210	540.5	−1465
		1.517	0.734	0.783	1.723	−14.24	−13.08	−11.78	10.62	0.110	535.0	−682.1
20	C9═O3	1.210	0.409	0.801	3.046	−21.26	−29.73	−26.67	35.13	0.115	1616.3	−3812
		1.210	0.421	0.789	2.877	−15.27	−28.04	−24.93	37.70	0.124	20260.1	−3636
21	C9—O2	1.326	0.479	0.847	2.299	−27.12	−18.67	−17.70	19.25	0.054	759.8	−2258
		1.326	0.459	0.867	2.156	−16.53	−18.23	−17.96	19.66	0.015	1330	−2210
22	O2—H9	1.004	0.775	0.227	2.107	−26.39	−31.06	−30.93	35.60	0.004	604.2	−1927
		1.001	0.793	0.209	2.257	−56.19	−37.83	−37.26	18.91	0.015	1695	−1861

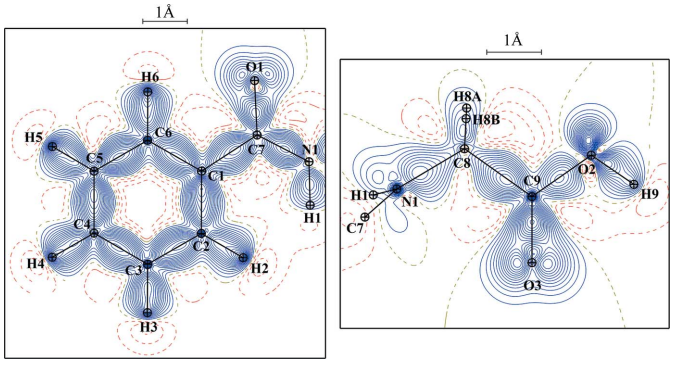

Figure 7
Static deformation density maps for (left) the ring part of the HA molecule and (right) the chain part, after experimental multipolar refinement. Contour level 0.05 e Å^{-3}.

the HA molecule, depicting the positions of the covalent BCPs in the molecule. The electron-density $\rho_{BCP}(\mathbf{r})$ and Laplacians of the electron density at all the BCPs of the HA molecule were calculated and compared with the corresponding theoretical calculations (Table 3).

3.3.1. Electron density. The positions of all BCPs, notably in homonuclear C—C bonds, are at the middle of the bonds, while in heteronuclear bonds (C—H, C—O, C—N, O—H) the BCPs stay away from the middle and are close to the electropositive atom (Fig. S2). In homonuclear C—C bonds, the electron densities $\rho_{BCP}(\mathbf{r})$ of the C5—C6 (2.208/2.112 e Å^{-3}) and C2—C3 (2.200/2.096 e Å^{-3}) bonds are slightly higher than the average value (∼2.157/2.091 e Å^{-3}) of the electron densities at the BCPs of the benzene ring of the HA molecule. This indicates that the charge density has shifted towards the C5—C6 and C2—C3 BCPs from the

neighbouring bonds of the benzene ring. The electron density $\rho_{BCP}(\mathbf{r})$ of the C1—C7 bond is higher (1.862/1.782 e Å^{-3}) than that of C8—C9 (1.752/1.723 e Å^{-3}) from the chain part of the HA molecule.

From the heteronuclear bonds, the electron densities of the bonds of the two carbonyl groups, C9═O3 and C7═O1, are 3.046/2.877 and 2.768/2.635 e Å^{-3}, respectively. This shows that electron density is more concentrated in C9═O3 of the two carbonyl groups of the HA molecule, while the $\rho_{BCP}(\mathbf{r})$ of C9—O2 is smaller (2.299/2.156 e Å^{-3}) than that of the carbonyl groups. Among the C—N bonds of the HA molecule, the $\rho_{BCP}(\mathbf{r})$ of the C7—N1 amide bond has a higher concentration (2.396/2.299 e Å^{-3}) of electron density at the BCPs compared with the electron density of the adjacent C8—N1 (1.896/1.807 e Å^{-3}). The O—H and N—H bonds of the HA molecule contain electron densities of 2.107/2.0257 and 2.146/2.288 e Å^{-3}, respectively. The electron density of the C—H bonds contained in the benzene ring of the HA molecule (∼1.845/1.935 e Å^{-3}) is higher than that of the C—H bonds in the CH_2 group (∼1.781/1.908 e Å^{-3}).

3.3.2. Laplacian of electron density. The Laplacian $\nabla^2\rho_{CP}$ of the electron density is the second derivative of the electron density $\rho_{BCP}(\mathbf{r})$ and tells us about the nature of the chemical bonding in a molecule (Koch & Popelier, 1995). If the Laplacian of the electron density $\nabla^2\rho_{CP} < 0$, then the charges are concentrated locally and the type of interaction is an 'open shell', whereas if $\nabla^2\rho_{CP} > 0$ then the charges are depleted locally and the type of interaction is 'closed shell'.

Fig. 8 shows the Laplacian map $\nabla^2\rho_{CP}$ of the HA molecule. The experimental Laplacians of electron density $\nabla^2\rho_{CP}$ were calculated and compared with the corresponding theoretical values (Table 3). In the present study, the Laplacians of the C—C bonds of the benzene ring range from −16.73/−20.36 to −21.52/−21.51 e Å^{-5} (experimental/theoretical). The Laplacian of C5—C6 is the highest, at −21.52/−21.51 e Å^{-5}, and this difference is due to the neighbouring carbonyl group. The C1—C7 bond has a Laplacian of electron density of −15.06/−15.37 e Å^{-5}, which is higher than that of C8—C9 at −14.11/−14.24 e Å^{-5} from the C—C bond in the chain part of the HA molecule. This higher Laplacian of electron density at the BCP of C1—C7 is because of the presence of the adjacent amide group.

Among the Laplacians of the C—N bonds, the Laplacian of C7—N1 has a much higher value of −29.05/−27.27 e Å^{-5} compared with the Laplacian of electron density of C8—N1 at −12.15/−17.36 e Å^{-5}, depicting the effect of a higher concentration of electron density at C7—N1. The higher electron density at C7—N1 is probably on account of the electron-donating resonance effect of the lone pair of electrons on the N atom to the atom O1.This significant difference in Laplacian values may also indicate that C7—N1 is responsible for the *trans* conformation of C7═O1 and N1—H1 (Pauling *et al.*, 1951), while the depleted Laplacian of C8—N1 is because of locally bonded C—H bonds.

For the two carbonyl groups, the Laplacian of electron density $\nabla^2\rho_{CP}$ of C9═O3 is −21.26/−15.27 e Å^{-5}, higher than the Laplacian of C7═O1. The Laplacian of electron density of hydroxyl group O2—H9 is −26.39/−56.19 e Å^{-5}, which is quite high, thus indicating the highly polar nature of the O2—H9 bond in the HA molecule. The Laplacian of N1—H1 is −28.94/−39.49 e Å^{-5}, indicating that it contains a much higher concentration of electron density.

The Laplacians of the C—H bonds in the benzene ring have an average value of ∼−16.23/−24.74 e Å^{-5}, a higher value than the Laplacians of the C—H bonds in the chain part of the HA molecule. The Laplacians of C8—H8*A* (−16.52/−19.29124.71 e Å^{-5}) and C8—H8*B* (−15.94/−24.77 e Å^{-5}) are unequal, showing that the bonding arrangements of these two H atoms are not same.

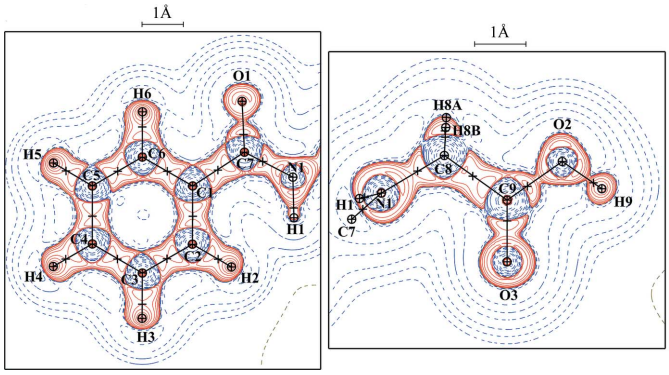

Figure 8
A map of the Laplacian of electron density for (left) the ring part of the HA molecule and (right) the chain part for the experimental model, showing the covalent bond-critical points.

3.4. Electron density of intermolecular interactions

In the crystal structure of HA, all the heteroatoms, *i.e.* O1, O2, O3 and N1, form intermolecular interactions with neighbouring molecules. Therefore a critical-point (CP) search of all inter- and intramolecular interactions gave a (3,−1) critical point for O—H···O, N—H···O and C—H···O hydrogen bonding. Further, topological analysis of the electron density at the CPs of the above interactions has a positive Laplacian (Gatti, 2005; Grabowski, 2006).

Among all the intermolecular interactions, the O—H···O hydrogen-bonding interaction joins two molecules of the asymmetric unit, while the other two are joined by N—H···O hydrogen-bonding interactions. The O—H···O hydrogen-bonding interaction joins the two molecules *via* O2—H9···O1^{i} [1.826 Å; symmetry code: (i) $x+\frac{1}{2}, -y+\frac{3}{2}, -z+2$] with an electron density $\rho_{BCP}(\mathbf{r})$ = 0.228/0.277 e Å^{-3} and the corresponding Laplacian of electron density $\nabla^2\rho_{CP}$ = 5.169/3.447 e Å^{-5}, while the bond kinetic and potential energy values are 120.51/90.23 and −100.22/−86.56 kJ mol^{-1} Bohr^{-3}, respectively (Table 4). All the intermolecular hydrogen-bonding interactions fulfil the criterion $\nabla^2\rho_{CP} > 0$, confirming that they are closed-shell interactions that are more ionic in nature (Gilli *et al.*, 1994; Espinosa & Molins, 2000; Espinosa *et al.*, 2002). Because of the quite elevated Laplacian value and electron-density concentration, the O—H···O interactions

Table 4
Topological properties of (3, −1) CPs in the intermolecular interactions: distances (Å), electron density (e Å^{-3}), Laplacian (e Å^{-5}), Hessian eigenvalues (e Å^{-5}), ε = ellipticity, G_{CP} = bond kinetic-energy density (kJ mol^{-1} Bohr^{-3}) and V_{CP} = bond potential-energy density (kJ mol^{-1} Bohr^{-3}).

No.	Interacting atoms	d_{12}	d_{1CP}	d_{2CP}	$\rho_{BCP}(r)$	$\nabla^2\rho$(BCP)	λ_1	λ_2	λ_3	ε	G_{CP}	V_{CP}
1	O2—H9···O1^{i}	1.672	0.559	1.120	0.228	5.169	−1.22	−1.21	7.6	0.004	120.51	−100.22
		1.675	1.125	0.550	0.277	3.447	−1.617	−1.564	6.628	0.033	90.23	−86.56
2	N1—H1···O1^{ii}	1.991	0.738	1.289	0.099	2.322	−0.48	−0.39	3.19	0.222	48.81	−34.38
		1.995	1.262	0.735	0.147	1.728	−0.634	−0.594	2.957	0.067	47.43	−47.78
3	C8—H8B···O3^{iii}	2.540	1.013	1.537	0.036	0.691	−0.13	−0.12	0.93	0.079	13.75	−8.68
		2.539	1.537	1.003	0.056	0.658	−0.191	−0.185	1.034	0.033	16.10	−14.29
4	C4—H4···O2^{iv}	2.575	1.163	1.456	0.053	0.783	−0.18	−0.17	1.14	0.026	16.57	−11.82
		2.573	1.091	1.494	0.059	0.788	−0.188	−0.154	1.130	0.227	18.42	−15.37
5	C4—H4···O3^{v}	2.639	1.201	1.495	0.038	0.605	−0.11	−0.1	0.81	0.076	12.33	−8.18
		2.636	1.124	1.518	0.042	0.599	−0.127	−0.104	0.830	0.220	13.53	−10.77
6	C3—H3···O3^{vi}	2.705	1.190	1.544	0.037	0.541	−0.12	−0.11	0.78	0.137	11.12	−7.49
		2.705	1.154	1.567	0.039	0.542	−0.112	−0.094	0.748	0.187	12.18	−9.598
7	C3—H3···O2^{ii}	3.075	1.400	1.729	0.021	0.291	−0.06	−0.05	0.4	0.056	5.78	−3.64
		3.196	1.413	1.785	0.040	0.594	−0.125	−0.102	0.821	0.222	13.20	−10.37

Symmetry codes: (i) $x+\frac{1}{2}, -y+\frac{3}{2}, -z+2$; (ii) $-x+1, y-\frac{1}{2}, -z+\frac{3}{2}$; (iii) $x-\frac{1}{2}, -y+\frac{3}{2}, -z+2$; (iv) $x, y, z-1$; (v) $-x+\frac{1}{2}, -y+1, z+\frac{1}{2}$; (vi) $-x+\frac{3}{2}, -y+1, z-\frac{1}{2}$.

are considered to be the strongest hydrogen-bonding interactions in the crystal structure.

In the same way, the N—H···O interaction joins two molecules via N1—H1···O1^{ii} [1.289 Å; symmetry code: (ii) $-x+1, y-\frac{1}{2}, -z+\frac{3}{2}$] with an electron density $\rho_{BCP}(\mathbf{r})$ = 0.099/0.147 e Å^{-3} and a corresponding Laplacian of electron density $\nabla^2\rho_{CP}$ = 2.322/1.728 e Å^{-5}, while the bond kinetic and potential energy values are 48.41/47.43 and −34.38/−47.78 kJ mol^{-1} Bohr^{-3}, respectively (Table 4), indicating moderately strong quasicovalent-type bonding among the intermolecular interactions in the crystal structure.

In the O2—H9···O1^{i} and N1—H1···O1^{ii} interactions, atom O1 of carbonyl C7═O1 is bifurcated (Jeffrey & Saenger, 2012) between the two, acting as a bifurcating acceptor (Desiraju & Steiner, 2001). Among all the C—H···O interactions, the C8—H8*B*···O3^{iii} (Table 4) intermolecular interaction is the strongest as the electron density $\rho_{BCP}(\mathbf{r})$ and the Laplacian of electron density are 0.036/0.056 e Å^{-3} and 0.691/0.658 e Å^{-5}, respectively. A cluster of the interacting molecules with the parent molecule, showing the bond paths and intermolecular critical points, is shown in Fig. 9.

3.5. Gradient vector field and atomic charges

The difference between the electronic and nuclear charges integrated over the atomic basins defined by zero-flux surfaces is called the 'atomic charge' (Bader, 1985). The Bader atoms-in-molecules (AIM) atomic charges of the atoms in HA were calculated experimentally and theoretically using *WinXPRO* (Version v.3x; Stash & Tsirelson, 2014) and are in good agreement with their chemical nature and bonding environment (Table 5). Fig. 10 shows the gradient vector field of electron density $\nabla\rho(r)$ of the HA molecule.

The zero-flux surfaces of AIM define the boundary of an atomic basin (Bader, 1985). The highly electronegative O atoms and an N atom represent large volumes compared with the C atoms. The atomic basins of the O atoms are drop-shaped while those of the C atoms have a prismatic shape. Because of the aspherical valence electron density (Coppens, 1997), the gradient trajectory lines are dominant at the core of the basins and decrease with increasing distance from the nucleus. In the present study, in the amide bond N1—C7 of the HA molecule, atom N1 carries a high negative charge

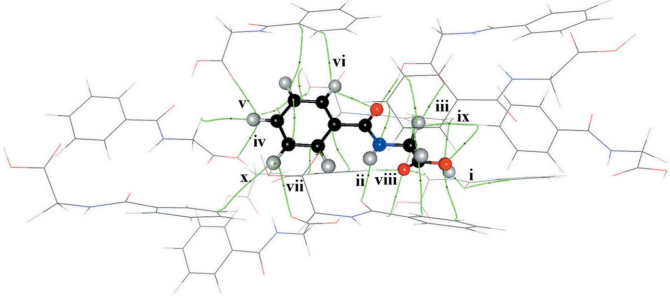

Figure 9
A cluster of HA molecules around the reference molecule, showing the intermolecular bond paths (green lines) and critical points (dots). Some of the symmetry codes are given in Table 2.

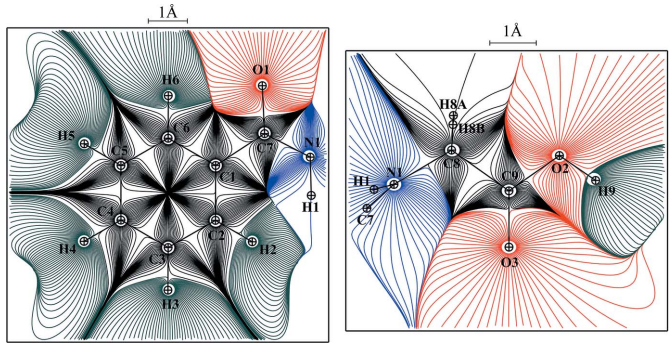

Figure 10
The gradient vector fields, showing the atomic basins of individual atoms for the experimental model.

Table 5
Atomic charges and atomic volumes.

MM denotes results from the multipolar model and DFT those from density functional theory.

	Charge (q)		Volume (Å^3)	
Atom	MM	DFT	MM	DFT
C1	−0.072	−0.030	11.19	10.76
C2	−0.195	−0.036	12.19	11.45
H2	0.156	0.063	5.438	5.718
C3	−0.047	−0.034	12.01	12.34
H3	0.203	0.071	7.625	8.143
C4	−0.059	−0.011	12.42	12.12
H4	0.184	0.065	6.650	7.063
C5	−0.170	−0.028	13.39	12.38
H5	0.134	0.064	6.418	6.722
C6	0.001	−0.044	11.54	11.72
H6	0.097	0.067	6.912	6.681
C7	1.424	1.388	5.198	6.036
C8	0.420	0.336	7.513	7.946
H8*A*	0.120	0.081	6.208	6.677
H8*B*	0.135	0.104	6.213	5.835
C9	1.596	1.604	4.515	5.186
N1	−1.339	−1.212	14.07	13.10
O1	−1.161	−1.213	16.10	16.86
O2	−1.268	−1.187	18.86	18.35
O3	−1.260	−1.185	19.26	19.26
H1	0.526	0.483	2.413	2.756
H9	0.581	0.655	1.949	1.621

(−1.339 e/−1.212 e) (experimental/theoretical). This high negative charge tends to have a high positive charge on its attached C7 atom [1.424 e/1.388 e], making the bond polar. The shape of atom N1 is triangular prismatic and has a large volume (14.07/13.10 Å^3), while that of C7 has a small volume (5.198/6.036 Å^3) among all the C atoms in HA molecule. Atom C8 bonded to atom N1 of the amide bond also has a small volume (7.513/7.946 Å^3) with the polarity of charge being 0.420 e/0.336 e.

Among the O atoms, O3 has the largest volume (19.26/19.26 Å^3) and carries the expected highly negative charges (−1.260 e/−1.185 e), as it is strongly involved in hydrogen-bonding interactions in the HA molecule. In the same way, atoms O2 and O1 are also involved in relatively strong hydrogen-bonding interactions as they have large volumes (18.86/18.35 Å^3 and 16.10/16.86 Å^3, respectively) and a higher level of atomic charges (−1.268 e/−1.187 e and −1.161 e/−1.213 e, respectively). The volumes and atomic charges of the O atoms in the HA molecule are in the order O3 > O2 > O1.

The charges on carbonyl atom C9 are more positive (1.596 e/1.604 e) and it has a smaller volume (4.515/5.186 Å^3) as it is bound to the highly negative atom O3.

In the benzene ring of the HA molecule, the atomic basins of the C atoms have a prismatic shape, in which C2 and C5 carry relatively more negative charge (−0.195 e/−0.036 e and −0.170 e/−0.028 e, respectively) and have volumes of 12.19/11.45 Å^3 and 13.39/12.38 Å^3, respectively.

The H atoms of the HA molecule show significant differences in their volumes and in their atomic charges. The charges on H9 (0.581 e/0.655 e) and H1 (0.526 e/0.483 e) are more positive than those on the other H atoms because they

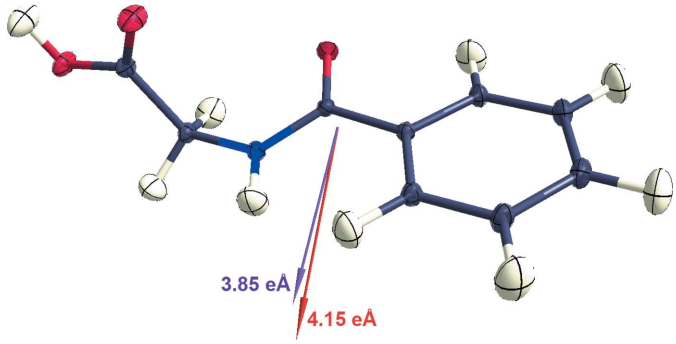

Figure 11
The dipole-moment vectors and their direction. Red indicates the experimental value and purple the theoretical.

are bonded to the electronegative O2 and N1 atoms and involved in strong hydrogen-bonding interactions (Matta & Hernández-Trujillo, 2003; Desiraju & Steiner, 2001).

It is concluded that, among all the atoms in the HA molecule, atoms C7 and C9 exhibit the most positive charges (1.424 e/1.388 e and 1.596 e/1.604 e, respectively), while atoms O3 and N1 carry the most negative charges (−1.260 e/−1.185 e and −1.339 e/−1.212 e, respectively). This higher concentration of positive and negative charges determines the polarity of the bond that is significantly involved in hydrogen-bonding interactions. Thus, C7, C9, O3 and N1 are atoms with higher atomic charges, making them the main cause of hydrogen-bonding interactions in the HA molecule. The atomic charges of these atoms enable the HA to bind at site II of serum albumin protein with high affinity.

Dipole moment is used as a parameter to study the drug/metabolite–receptor interaction (Lien *et al.*, 1982). The dipole-moment values and charge-density distribution are also related to biological activity (Dittrich & Jayatilaka, 2012). In the present study, there is good agreement between the experimental and theoretical dipole-moment values. The experimental dipole-moment value for the HA molecule is 4.15 (2) e Å and the value obtained from solid-state theory calculation is 3.85 (2) e Å, which shows that the molecule is highly polar in nature. Fig. 11 shows the direction and strength of the dipole-moment vectors for the theoretical and experimental results.

3.6. Electrostatic potential and binding affinity

Electrostatic potential (ESP) is physically observable, one of the derived electrostatic properties of a molecule which is created by electrons and a system of nuclei and formulated directly from Coulomb's law (Murray & Politzer, 2011). The ESP of a molecule gives ample information on the binding ability of the molecule with neighbouring molecules, as well as the binding of a ligand with the active site of proteins and enzymes (Zhurova *et al.*, 2016, 2009; Kalaiarasi *et al.*, 2016; Rajalakshmi, Hathwar & Kumaradhas, 2014*a*,*b*; Rajalakshmi, Pavan & Kumaradhas, 2014; Arputharaj *et al.*, 2012; Fournier *et al.*, 2009; Dominiak *et al.*, 2007; Yearley *et al.*, 2007; Zhurova *et al.*, 2006). It allows the molecular recognition of a drug molecule in a drug–receptor interaction to be predicted and,

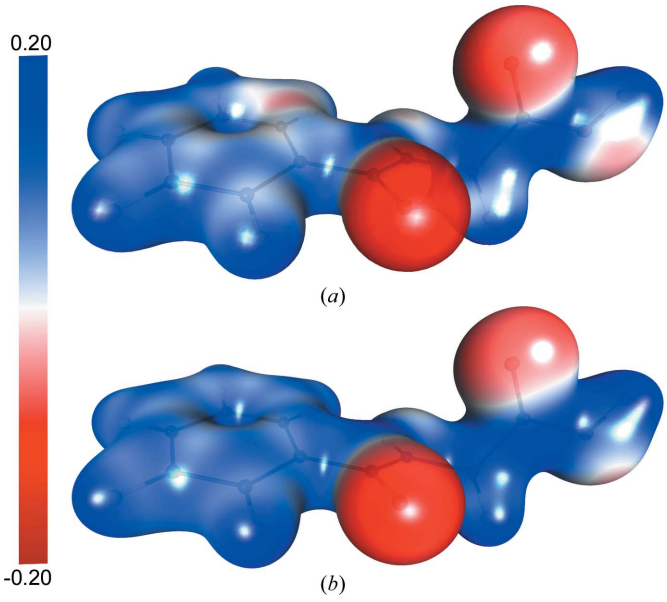

Figure 12
A three-dimensional electron-density surface of the HA molecule, coloured according to the electrostatic potential. (*a*) Experimental plot and (*b*) theoretical plot. Contour level 0.2 e Å^{-3}

more specifically, it allows the identification of the reactive site of a molecule in the biological environment. This information shows the mechanism of binding of a molecule with a particular receptor site in that biological environment. Thus, to get a better perspective of the binding mechanism of the HA molecule, the ESP surface of this molecule was analysed.

The experimental ESP isosurface is illustrated in Fig. 12, showing the highly electronegative and electropositive regions of the HA molecule. The vicinity of atom N1 (see Fig. 12) is surrounded by a negative ESP region and atom C7 by a positive ESP region. Atom C7 is bonded to the highly electronegative atom O1, thus making C7 more electrophilic and susceptible to attack by a nucleophile. In the same way, atom C9 is bonded to two highly electronegative atoms, C9—O2 and C9═O3. This makes atom C9 more electrophilic and liable to nucleophilic attack. The carbonyl O atoms in HA can only be hydrogen-bond acceptors, the hydroxyl group can be a donor or an acceptor and atom N1 of the amide bond can be a donor or an acceptor. The highly negative regions will clearly accept hydrogen bonds, whereas the C and H atoms will be potential donor sites with positive ESP. Therefore, the propensity of hydrogen bonding with regard to ESP region explains the binding mechanism.

Apart from this, the electronegative regions 'above' the aromatic ring where the expected π electrons are seen to be present act as nucleophiles, while the electropositive regions 'below' the aromatic ring act as electrophiles, as depicted in the ESP surface of the HA molecule (Fig. 12). Thus, the substituents that increase the electron density in the HA ligand appear to increase the binding affinity. The most striking observation from the ESP distribution of the HA molecule is that for high binding affinity to either site I or site II of the serum albumin protein receptor, the negative ESP areas have to be extensive and large. Large negative ESP areas are found enveloping the O atoms of the carbonyl and hydroxyl groups and the N atom of the amide bond. These extensive highly pronounced negative regions of ESP result in the high binding affinity of the HA ligand at site II of the human serum albumin protein which is mainly surrounded by hydrophilic residues. The negative ESP region is only found above the aromatic region and is not very pronounced compared with the chain part of the HA ligand. The observed negative ESP above the aromatic ring is a measure of the potential interaction of HA at site I of human serum albumin. Thus, only the negative ESP region of the aromatic ring shows an intermediate relative binding effect with low affinity at site I of the human serum albumin protein.

Studies of the molecular docking of HA and HSA (Zaidi *et al.*, 2013) reveal that site I of HSA is composed of Lys199, Arg222, Tyr150, Glu153, Ser192, Lys195, Gln196 Trp214, His242, Arg257, Ala291 and Glu292, while site II consists of Leu387, Ile388, Asn391, Cys392, Leu407, Arg410, Tyr411, Leu430, Val433, Cys438, Ala449 and Leu453 amino acid residues. Arg410 and Tyr411 are the crucial amino acid residues present in the centre of the drug-binding site II of HSA (Watanabe *et al.*, 2000) and are capable of forming strong interactions and thus of being involved in the high-affinity binding of HA with site II.

4. Conclusions

The present work has reported a detailed experimental charge-density analysis of hippuric acid (HA) and the results have been compared with those obtained from DFT calculations. The critical question of the preferred binding of HA with one of the two drug-binding sites of human serum albumin (HSA), resulting in the hindered elimination of this uremic toxin, has been addressed. The molecular surface comprises a ring part and a chain part. Compared with the former, the latter part has very strong interaction sites and can form strong classical hydrogen bonds. Topological analysis of O—H···O, N—H···O, C—H···O types of hydrogen-bond interactions explains the nature of the intermolecular interactions that can most likely occur when HA encounters HSA in the biological environment.

The presence of highly electronegative atoms O1, O2 and O3 with a very negative electrostatic potential, as well as the higher negative values of the corresponding atomic charges, enables HA to bind preferentially with site II of HSA in the biological environment. The ring contains only a small region with a negative electrostatic potential which might be involved in site-specific binding of the HA molecule, but its binding affinity with site I of HSA is presumed to be much lower than that of the chain part.

Thus, this charge-density study of the HA molecule has enabled us to understand the preferred binding regions. It would be worth studying the crystal structure of serum albumin protein bound with HA at reasonable resolution to verify the results discussed above.

Acknowledgements

The authors gratefully acknowledge the Higher Education Commission and the Federal Government of Pakistan for funding under the Public Sector Development Programme to establish the Materials Chemistry Laboratory at The Islamia University of Bahawalpur, Pakistan, which made this study possible.

References

Allen, F. H. & Bruno, I. J. (2010). *Acta Cryst.* B**66**, 380–386.
Altomare, A., Cascarano, G., Giacovazzo, C. & Guagliardi, A. (1993). *J. Appl. Cryst.* **26**, 343–350.
Arputharaj, D. S., Hathwar, V. R., Guru Row, T. N. & Kumaradhas, P. (2012). *Cryst. Growth Des.* **12**, 4357–4366.
Bader, R. F. (1985). *Acc. Chem. Res.* **18**, 9–15.
Bhattacharya, A. A., Curry, S. & Franks, N. P. (2000). *J. Biol. Chem.* **275**, 38731–38738.
Bouhmaida, N., Bonhomme, F., Guillot, B., Jelsch, C. & Ghermani, N. E. (2009). *Acta Cryst.* B**65**, 363–374.
Boumendil-Podevin, E. F., Podevin, R. A. & Richet, G. (1975). *J. Clin. Invest.* **55**, 1142–1152.
Bruker (2016). *APEX3*, *SAINT* and *SADABS*. Bruker AXS Inc., Madison, Wisconsin, USA.
Clementi, E. & Roetti, C. (1974). *At. Data Nucl. Data Tables*, **14**, 177–478.
Coppens (1997). *X-ray Charge Densities and Chemical Bonding*. IUCr Texts on Crystallography, No. 4. Oxford University Press.
Desiraju, G. R. & Steiner, T. (2001). *The Weak Hydrogen Bond in Structural Chemistry and Biology*. *IUCr Monographs on Crystallography*, Vol. 9. Oxford University Press.
Dittrich, B. & Jayatilaka, D. (2012). *Electron Density and Chemical Bonding II*, pp. 27–45. Heidelberg: Springer.
Dominiak, P. M., Volkov, A., Li, X., Messerschmidt, M. & Coppens, P. (2007). *J. Chem. Theory Comput.* **3**, 232–247.
Duranton, F., Cohen, G., De Smet, R., Rodriguez, M., Jankowski, J., Vanholder, R., Argiles, A. & European Uremic Toxin Work Group (2012). *J. Am. Soc. Nephrol.* **23**, 1258–1270.
Dzúrik, R., Spustová, V., Krivošíková, Z. & Gazdíková, K. (2001). *Kidney Int.* **59**, S278–S281.
Espinosa, E., Alkorta, I., Elguero, J. & Molins, E. (2002). *J. Chem. Phys.* **117**, 5529–5542.
Espinosa, E. & Molins, E. (2000). *J. Chem. Phys.* **113**, 5686–5694.
Farrugia, L. J. (1997). *J. Appl. Cryst.* **30**, 565.
Flack, H. D. (1983). *Acta Cryst.* A**39**, 876–881.
Fournier, B., Bendeif, E. E., Guillot, B., Podjarny, A., Lecomte, C. & Jelsch, C. (2009). *J. Am. Chem. Soc.* **131**, 10929–10941.
Frisch, M. J., Trucks, G. W., Schlegel, H. B., Scuseria, G. E., Robb, M. A., Cheeseman, J. R., Scalmani, G., Barone, V., Mennucci, B., Petersson, G. A., Nakatsuji, H., Caricato, M., Li, X., Hratchian, H. P., Izmaylov, A. F., Bloino, J., Zheng, G., Sonnenberg, J. L., Hada, M., Ehara, M., Toyota, K., Fukuda, R., Hasegawa, J., Ishida, M., Nakajima, T., Honda, Y., Kitao, O., Nakai, H., Vreven, T., Montgomery, J. A. Jr, Peralta, J. E., Ogliaro, F., Bearpark, M. J., Heyd, J., Brothers, E. N., Kudin, K. N., Staroverov, V. N., Kobayashi, R., Normand, J., Raghavachari, K., Rendell, A. P., Burant, J. C., Iyengar, S. S., Tomasi, J., Cossi, M., Rega, N., Millam, N. J., Klene, M., Knox, J. E., Cross, J. B., Bakken, V., Adamo, C., Jaramillo, J., Gomperts, R., Stratmann, R. E., Yazyev, O., Austin, A. J., Cammi, R., Pomelli, C., Ochterski, J. W., Martin, R. L., Morokuma, K., Zakrzewski, V. G., Voth, G. A., Salvador, P., Dannenberg, J. J., Dapprich, S., Daniels, A. D., Farkas, Ö., Foresman, J. B., Ortiz, J. V., Cioslowski, J. & Fox, D. J. (2009). *GAUSSIAN09.2*. Gaussian Inc., Wallingford, Connecticut, USA.
Gatti, C. (2005). *Z. Kristallogr. Cryst. Mater.* **220**, 399–457.
Ghuman, J., Zunszain, P. A., Petitpas, I., Bhattacharya, A. A., Otagiri, M. & Curry, S. (2005). *J. Mol. Biol.* **353**, 38–52.
Gilli, P., Bertolasi, V., Ferretti, V. & Gilli, G. (1994). *J. Am. Chem. Soc.* **116**, 909–915.
Grabowski, S. J. (2006). Editor. *Hydrogen Bonding: New Insights*. *Challenges and Advances in Computational Chemistry and Physics*, Vol. 3. Dordrecht: Springer.
Grabowsky, S., Pfeuffer, T., Chęcińska, L., Weber, M., Morgenroth, W., Luger, P. & Schirmeister, T. (2007). *Eur. J. Org. Chem.* **2007**, 2759–2768.
Grabowsky, S., Pfeuffer, T., Morgenroth, W., Paulmann, C., Schirmeister, T. & Luger, P. (2008). *Org. Biomol. Chem.* **6**, 2295–2307.
Grimme, S., Antony, J., Ehrlich, S. & Krieg, H. (2010). *J. Chem. Phys.* **132**, 154104.
Hansen, N. K. & Coppens, P. (1978). *Acta Cryst.* A**34**, 909–921.
Hartwigsen, C., Goedecker, S. & Hutter, J. (1998). *Phys. Rev. B*, **58**, 3641–3662.
He, X. M. & Carter, D. C. (1992). *Nature*, **358**, 209–215.
Hirshfeld, F. L. (1976). *Acta Cryst.* A**32**, 239–244.
Hung, H. C. & Chang, G. G. (2001). *Biophys. J.* **81**, 3456–3471.
Hutter, J., Iannuzzi, M., Schiffmann, F. & VandeVondele, J. (2014). *WIREs Comput. Mol. Sci.* **4**, 15–25.
Jeffrey, G. A. & Saenger, W. (2012). *Hydrogen Bonding in Biological Structures.* Heidelberg: Springer-Verlag.
Jelsch, C., Ejsmont, K. & Huder, L. (2014). *IUCrJ*, **1**, 119–128.
Jelsch, C., Guillot, B., Lagoutte, A. & Lecomte, C. (2005). *J. Appl. Cryst.* **38**, 38–54.
Johnson, C. K. & Burnett, M. N. (1996). *ORTEPIII.* Report ORNL-6895. Oak Ridge National Laboratory, Tennessee, USA.
Kalaiarasi, C., Pavan, M. S. & Kumaradhas, P. (2016). *Acta Cryst.* B**72**, 775–786.
Koch, U. & Popelier, P. L. A. (1995). *J. Phys. Chem.* **99**, 9747–9754.
Krause, L., Herbst-Irmer, R., Sheldrick, G. M. & Stalke, D. (2015). *J. Appl. Cryst.* **48**, 3–10.
Lien, E. J., Guo, Z. R., Li, R. L. & Su, C. T. (1982). *J. Pharm. Sci.* **71**, 641–655.
Lu, T. & Chen, F. (2012). *J. Comput. Chem.* **33**, 580–592.
Madsen, A. Ø. (2006). *J. Appl. Cryst.* **39**, 757–758.
Manjula, S., Kalaiarasi, C., Pavan, M. S., Hathwar, V. R. & Kumaradhas, P. (2018). *Acta Cryst.* B**74**, 693–704.
Matta, C. F. & Hernández-Trujillo, J. (2003). *J. Phys. Chem. A*, **107**, 7496–7504.
McKinnon, J. J., Fabbiani, F. P. & Spackman, M. A. (2007). *Cryst. Growth Des.* **7**, 755–769.
McKinnon, J. J., Spackman, M. A. & Mitchell, A. S. (2004). *Acta Cryst.* B**60**, 627–668.
Miyamoto, Y., Iwao, Y., Tasaki, Y., Sato, K., Ishima, Y., Watanabe, H., Kadowaki, D., Maruyama, T. & Otagiri, M. (2010). *FEBS Lett.* **584**, 2816–2820.
Murray, J. S. & Politzer, P. (2011). *WIREs Comput. Mol. Sci.* **1**, 153–163.
Muzet, N., Guillot, B., Jelsch, C., Howard, E. & Lecomte, C. (2003). *Proc. Natl Acad. Sci. USA*, **100**, 8742–8747.
Niwa, T. (1996). *Semin. Nephrol.* **16**, 167–182.
Ohtsuki, S., Asaba, H., Takanaga, H., Deguchi, T., Hosoya, K. I., Otagiri, M. & Terasaki, T. (2002). *J. Neurochem.* **83**, 57–66.
Parsons, S., Flack, H. D. & Wagner, T. (2013). *Acta Cryst.* B**69**, 249–259.
Pauling, L., Corey, R. B. & Branson, H. R. (1951). *Proc. Natl Acad. Sci. USA*, **37**, 205–211.
Perdew, J. P., Burke, K. & Ernzerhof, M. (1996). *Phys. Rev. Lett.* **77**, 3865–3868.
Peters, T. Jr (1995). *All about Albumin. Biochemistry, Genetics, and Medical Applications*. New York: Academic Press.
Petitpas, I., Bhattacharya, A. A., Twine, S., East, M. & Curry, S. (2001). *J. Biol. Chem.* **276**, 22804–22809.

Rajalakshmi, G., Hathwar, V. R. & Kumaradhas, P. (2014*a*). *Acta Cryst.* B**70**, 331–341.
Rajalakshmi, G., Hathwar, V. R. & Kumaradhas, P. (2014*b*). *Acta Cryst.* B**70**, 568–579.
Rajalakshmi, G., Pavan, M. S. & Kumaradhas, P. (2014). *RSC Adv.* **4**, 57823–57833.
Ringertz, H. (1971). *Acta Cryst.* B**27**, 285–291.
Sheldrick, G. M. (2015). *Acta Cryst.* C**71**, 3–8.
Spackman, M. A. & Jayatilaka, D. (2009). *CrystEngComm*, **11**, 19–32.
Spustová, V., Gajdos, M., Opatrný, K., Stefíková, K. & Dzúrik, R. (1991). *Physiol. Res.* **40**, 599–606.
Stash, A. I. & Tsirelson, V. G. (2014). *J. Appl. Cryst.* **47**, 2086–2089.
Sudlow, G. D. J. B., Birkett, D. J. & Wade, D. N. (1975). *Mol. Pharmacol.* **11**, 824–832.
Sugio, S., Kashima, A., Mochizuki, S., Noda, M. & Kobayashi, K. (1999). *Protein Eng. Des. Sel.* **12**, 439–446.
Turner, M. J., McKinnon, J. J., Wolff, S. K., Grimwood, D. J., Spackman, P. R., Jayatilaka, D. & Spackman, M. A. (2017). *CrystalExplorer17*. University of Western Australia.
Vanholder, R., De Smet, R., Glorieux, G., Argilés, A., Baurmeister, U., Brunet, P., Clark, W., Cohen, G., De Deyn, P. P., Deppisch, R., Descamps-Latscha, B., Henle, T., Jörres, A., Lemke, H. D., Massy, Z. A., Passlick-Deetjen, J., Rodriguez, M., Stegmayr, B., Stenvinkel, P., Tetta, C., Wanner, C., Zidek, W. & European Uremic Toxin Work Group (EUTox) (2003). *Kidney Int.* **63**, 1934–1943.
Vanholder, R. C., De Smet, R. V. & Ringoir, S. M. (1992). *Clin. Chem.* **38**, 1429–1436.
Varshney, A., Rehan, M., Subbarao, N., Rabbani, G. & Khan, R. H. (2011). *PLoS One*, **6**, e17230.
Vega, D. & Almeida, D. (2014). *J. Comput. Methods Sci. Eng.* **14**, 131–136.
Watanabe, H., Tanase, S., Nakajou, K., Maruyama, T., Kragh-Hansen, U. & Otagiri, M. (2000). *Biochem. J.* **349**, 813–819.
Yearley, E. J., Zhurova, E. A., Zhurov, V. V. & Pinkerton, A. A. (2007). *J. Am. Chem. Soc.* **129**, 15013–15021.
Zaidi, N., Ajmal, M. R., Rabbani, G., Ahmad, E. & Khan, R. H. (2013). *PLoS One*, **8**, e71422.
Zhurova, E. A., Matta, C. F., Wu, N., Zhurov, V. V. & Pinkerton, A. A. (2006). *J. Am. Chem. Soc.* **128**, 8849–8861.
Zhurova, E. A., Zhurov, V. V., Chopra, D., Stash, A. I. & Pinkerton, A. A. (2009). *J. Am. Chem. Soc.* **131**, 17260–17269.
Zhurova, E. A., Zhurov, V. V., Kumaradhas, P., Cenedese, S. & Pinkerton, A. A. (2016). *J. Phys. Chem. B*, **120**, 8882–8891.
Zhurov, V. V., Zhurova, E. A. & Pinkerton, A. A. (2008). *J. Appl. Cryst.* **41**, 340–349.